J. Condensed Matter Nucl. Sci. 33 (2020) 126–144

Research Article

FCC Vacancies in ZrO_2PdD are the Active LANR Site

Mitchell R. Swartz*

JET Energy Inc., Wellesley Hills, MA 02481, USA

Abstract

Active lattice assisted nuclear reaction (LANR) systems emit very narrow bandwidth hyperfine radiofrequency (RF) emission peaks (ca. 327.37 MHz) signaling their LANR activity. This RF frequency is very close to the theoretical Deuteron-Line (DL; 327.348 MHz) proving that D is the fuel. Neither the maser emission, nor the revealing sidebands (superhyperfine structure) appear when the components are electrically driven at subthreshold voltage or when driven in electrical avalanche mode. The RF emission sidebands provide unique information about the conditions of the desired active LANR state.
 ISSN 2227-3123

Keywords: Cold fusion maser, Deuterium, Deuterium line, Free radical deuteron, Resonance broadening, Spectra, Superhyperfine, Superhyperfine lines, Vacancies

1. Overview of CF/LANR D-Line Hyperfine RF Emissions

Active lattice assisted nuclear reactions (LANR) systems, both aqueous and nanomaterial (ZrO_2 PdD preloaded Nanor®-type LANR components [1–12] operated carefully below their avalanche voltage[4]), emit very narrow bandwidth radiofrequency (RF) emission peaks (ca. 327.37 MHz), in the Deuteron-Line (DL; 327.348 MHz) region [13,14]. The high Q ($1.2–9 \times 10^6$) and Zeeman response indicate maser action. Higher applied voltages have revealed sidebands (superhyperfine line (SHFL) structure). These are non-Zeeman splitting because there are no additional significant applied H-fields. Analysis of the positions of the non-Zeeman SHFL splittings yields great insight into the LANR active site not otherwise available (Fig. 1). It is important that the RF DL hyperfine emissions come only from LANR (CF) active cells containing high loaded levels of deuterons.

Figure 1 is a four section analysis of the superhyperfine structure of Nanor®-type component 7-4 using a frequency–time plot. The top shows the actual SHFL sideband structure for Nanor®-type component #7-4, driven at ~10 V. This is a "waterfall" plot and intensity is shown as a function of frequency. The exact width of the SHFL splitting's dispacement, as a function of frequency, results from resonance broadening (RB) which occurs from perturbing deuterons located elsewhere, such as other vacancies, through energy exchange processes. RB impact was derived for the first four closest neighbor sites using the fact that the RB interaction decreases as $1/r^3$. As discussed in detail below, analysis such as shown in Fig. 1 demonstrates this nearest neighbor RB analysis. Here, the Nanor®-type

*Mitchell R. Swartz ScD, MD, EE, AC1ER, E-mail: drswartz@nanortech.com.

 ISSN 2227-3123

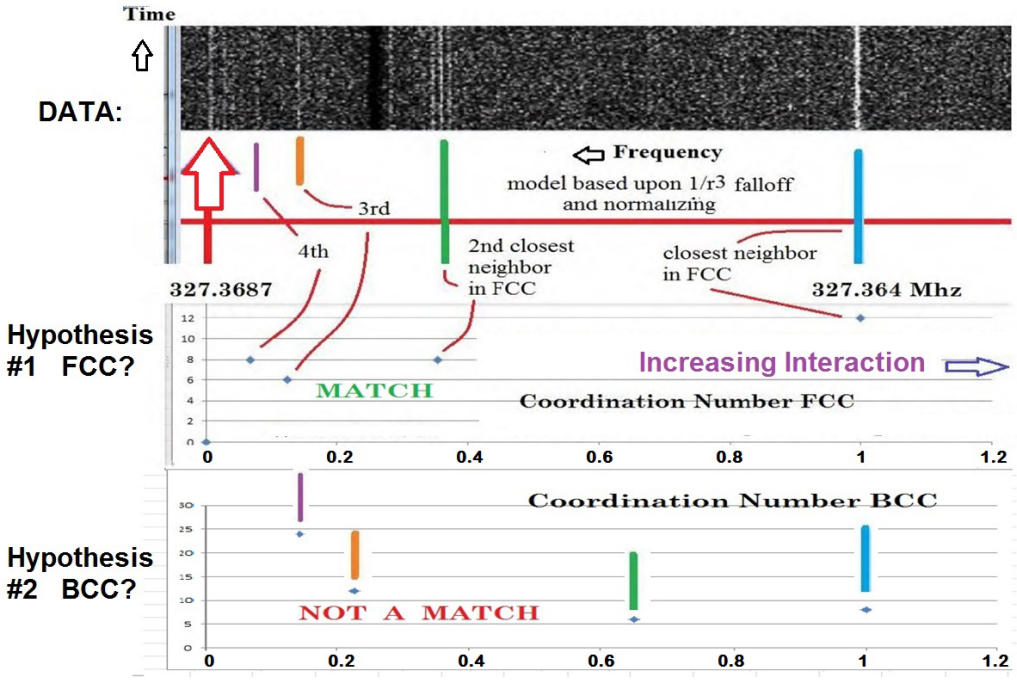

Figure 1. Analysis of an active ZrO_2PdD component's frequency–time plot.

component 7-4 is driven at sufficient voltage so that the additional SHF lines appear. Below, this is followed by assignments (labeled "Hypothesis") based upon nearest neighbor location and the expected resonance broadening falloff. The middle and bottom of the figure show the expected results for two different gendanken active sites: face and body centered cubic (FCC, BCC), respectively, both the coordination numbers (height) and expected deviation (to the right for frequency) are shown based upon known locations for both FCC and BCC lattice arrangements.

Figure 1 shows considerable overlap of the expected locations (in solid color) in the midgraph and the frequency singularities above them for the FCC lattice, but not the BCC lattice. It thus reveals that the key D* reactions occur in a lattice which is face center cubic (FCC). In Fig. 1, note the better overlap of the expected FCC locations in the midgraph, unlike the BCC lattice. The coordination numbers (CN) also better match for the FCC lattice. The location of the excited state deuterium is a vacancy within a slightly modified FCC lattice. The multiplet near the second nearest neighbor might herald that this is a zirconia at a rhombic corner (one phase of ZrO_2 is isoequivalent to a FCC vacancy) or an atom of zirconium (or other magnetic impurity) within the PdD lattice. This appears to confirm the prediction (ICCF-4 [16]) which also relates to the mechanism of fuel entering the active site – being a vacancy.

The results in nickel are more complex and demonstrate a range of FCC and body centered cubic (BCC) vacancies, possibly heralding new metallurgic phases. These discoveries add semiquantitative material science supporting theories that cite vacancies [16] as the site of the desired LANR reactions, with deuterons as its "fuel" to form *de novo* 4He.

Importantly, the D-line emission RF from active LANR systems confirms the role of atomic deuterium in LANR. It also heralds, and here identifies, the lattice connections between the loaded deuterons. This demonstrates that LANR active state's RF emission creates a new method to observe LANR systems, and especially LANR's difficult-to-attain

most-desired mode. The remainder of this paper is discussed these energy and matter power spectra.

2. Background

2.1. Hyperfine emission in radioastronomy

This effort links CF/LANR with the tools and methods of the science of radioastronomy which studies the universe by measuring RF emissions from several GHz to the far infrared. Together, the H-L and DL have provided understanding of the matter distribution through the known universe; providing information from post-Big Bang times just after recombination through reionization to the present. In radioastronomy, DL and HL observations have greatly improved human understanding of the extent, and interactions of galaxies, both now and back to a few hundred thousand years after the Big Bang.

2.2. Hyperfine emission from free radical hydrogen

The word deuterium indicates the deuteron has positive charge, but it is a charge neutral free radical with an unpaired electron. The energy states result from the interaction between the deuteron's electron's spin and its own nuclear spin. Deuterium is light enough that isospin is a good symmetry. The proton and neutron are both fermions, and a state containing two of them must be antisymmetric under exchange. The nuclear spin results from the fact that the proton and neutron interact by strong force. Because parallel electric currents attract, the parallel magnetic dipole moments (that is with antiparallel spins) has the lowest energy. The difference is a photon at 1420 MHz for hydrogen and 327.348 MHz for deuterium.

2.3. Long emission times heralded by narrow bandwidth

Because atomic deuterium and atomic hydrogen have no electric moment, the energy transition between the two states is highly forbidden. That means there is an extremely small transition rate of ~2.9×10^{-15} per second, which correlates to a mean lifetime of the excited state of ca. 10 million years. Therefore, simply put, a spontaneous transition between these states does not normally occur on Earth – unless induced using a hydrogen maser. But it is observed in astronomy. As a corollary, because of the long mean lifetime, the line has an extremely small natural width – as uniquely seen here.

3. Experimental

3.1. Materials – Aqueous nickel LANR system

There are three parts to the detection and analysis of the CF/LANR superhyperfine structure. First, the RF emissions are collected. Second, they are examined as a function of frequency, electric drive state, using ohmic and other controls. Finally, the data was examined to determine what type of loaded Group VIII lattice structure would produce the observed superhyperfine sideband structure. This is shown below for an active XSH-producing aqueous nickel CF/LANR system (MOAC type; "Mother of all Cathodes"), and for two dry preloaded palladium zirconia CF/LANR components (NANOR®-type).

Our first experimental surveys began with preliminary amateur radio and LANR investigations that examined and resolved, for the first time, the apparent absence of Hydrogen Line (HL) and presence of Deuterium Line (DL) emissions from the MOAC LANR (ordinary water) aqueous system electrically driven during its active mode [17,18]. The MOAC cell has a 3 l capacity with a cathode weighing 2.132 kg (#46 hard drawn smooth nickel wire with an area of ca. 240,000 cm^2). The electrolyte was a dilute carbonate solution in laboratory distilled deionized "ordinary" water. For the calorimetry, calibration was determined by ohmic controls and other methods, as discussed elsewhere [19–32].

3.2. Dry, preloaded LANR NANOR®-type components

The second investigations were a preliminary set of experiments looking for possible solid-state LANR maser action at 327.7 MHz (such as in Fig. 1) resulting from electrically driving ZrO_2PdD preloaded Nanor®-type LANR components [1–12], carefully below their avalanche voltage [4] when excess heat is known to cease. These LANR systems examined are two-terminal component with a cylindrical shape and active CF/LANR core.

The dry, preloaded nanocomposite components have at their core ZrO_2–PdD nanostructured material. They are smaller than 2 cm length, with 30–200 mg of active LANR material. Although small in size, the LANR excess power density is more than 19,500 W/kg of nanostructured material. The small, preloaded, dry components have enabled the way to higher instantaneous power gain, total energy gain, imaging, emissions, open demonstrations, and a better understanding of the impact of applied magnetic fields, and electrical transconduction [1–12].

Our previous studies and reports have been directed to both avoiding the avalanche voltage and approaching the optimal operating point (OOP) of the system [31]. Most importantly, we have demonstrated that several electrical transconduction states exist, but that only one is active, desired, and capable of producing "excess heat" [10,18,25]. Beyond the region of electrical avalanche, the previously active preloaded LANR quantum electronic components give a thermal output similar to a standard ohmic control (a carbon composition resistor). Despite driving at higher input electrical power, on other side of the electrical avalanche, these NANOR®-type components act as little more than electrical resistors which – when in electrical avalanche mode – are conventionally dissipative, not over-unity, and therefore are functionally "dead" with respect to producing excess heat.

3.3. Methods – RF emission detection system

Figure 2 shows the arrangement of detecting the RF emissions. SDR receivers (RTL-brand and the like) were used because of their high dynamic range, high bandpass stability, and excellent out-of-band rejection. The images shown are dynamic gradient with time markers on the left-hand side. The sample rate was 3.2 million samples per second (MSPS). Upper sideband (USB) was used to minimize imaging. Resolution was the highest achievable with a Blackman–Harris 4 window, although Bo Gardmark suggests using Hann or Hamming windows for improved signal to noise ratio (SNR) along with a AD8317 log detector.

The sensitivity of this detection system (SNR) is proportional to $A\sqrt{t}$, where A is the antenna's collecting area, and t is the integration time. What is not explicitly shown in Fig. 4, but is therefore quite important, is that the data is meticulously collected over several minutes to hours, as it is integrated/analyzed over time and as a function of frequency.

The LANR-emitted RF signals are weak, and therefore the antenna is made with an aperture as large as possible, and the collection is for as long a time as possible. Current investigations use three antennae: reflector, Yagi, and a convenient "duck" antenna system. The latter fit easily into the resonance chamber. Although often ignored, the antenna feed line loss was significant and had to be addressed for this iteration of experimental runs. The coaxial improvement for this version (CNT400) was significant with 90 db gain per standardized length.

3.4. Resonant chamber

A 36 inch long metallic case was used as the resonant cavity with the half wavelength set vertically. It contains the antenna, beginning of transmission line, and NANOR® type component. A white envelope is used, surrounding the NANOR®-type CF/LANR component to easily detect, and to protect against, falling or extravasated nanomaterials. For the experiment, the door was shut, sealed, covered with aluminum foil and connected to a driven copper rod driven into the Earth.

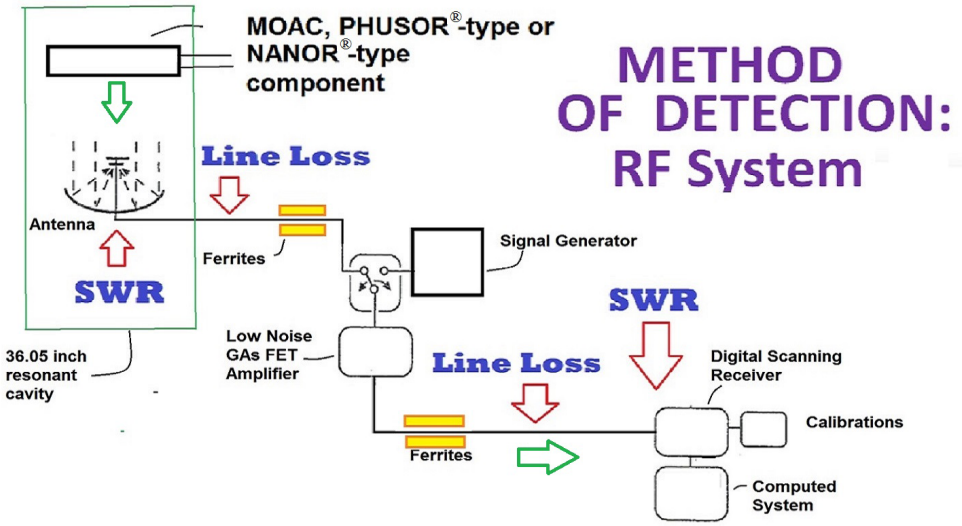

Figure 2. Block diagram of the system used for the HL and DL receiver system. Shown is a block diagram representation for the CF/LANR emitter, the antenna, line feeds and transmission lines (including serious line loss), the ferrites, the control signal generator, the Gas FET amplifier, the most relevant standing wave ratio (SWR) points to match, computation and software defined receiver (SDR). The use of antenna analyzers and matching decreased the SWR from ca. 20+ to 2–3. The use of military grade coax (CNT400) decreased the transmission line loss by +90 db, and the low noise amplifier (LNA) provided an additional +20 db gain. Ferrites are used to minimize shield currents and radio frequency interference (RFI) from nearby active equipment.

3.5. Galactic control

Interference has been considered, and eliminated, by monitoring over several weeks, and comparison to known frequency dispersions and examination of bandwidth. Changes as a function of time and/or frequency have led to the identification of modulated (military in this band) signals, and galactic input. Possible television transmitters, cell phones, microwave appliances, and ionospheric noise (QRN) have not been a significant problem at these frequencies given the long term monitoring and pre-identification. Investigators should use well-ground Faraday cages, and are advised that it may take weeks to understand the background. However, not having a detailed understanding of the vast background does not preclude using the D-line to monitor and better understand CF/LANR.

For each experiment, attention has been necessarily made to the location of the Galactic center, and, when possible, measurements have been made when the Earth is optimally shielding emissions from the galactic center. This was found to be much less needed once the resonator box was correctly grounded. As background, the Galactic center continuum is reported to have nonthermal background of ~500 K (with a 25 element sub-array, 23 dB gain, 12° beam width, 12 m^2 effective aperture). The Galactic anticenter has a non-thermal background of ~70 K and, therefore, any deuterium excitation temperature $\geq$130 K causes appearance of RF emissions.

3.6. Ohmic controls

In this case, for this paper, the controls included having nothing in the Faraday cage with full double shielding as discussed above, and included having the NANOR® type component present in the cage but being NOT electrically driven. In addition, controls included having in the same electrical circuit an electrically driven ohmic control instead

of the NANOR® type component. In this case, the ohmic control consisted of a carbon resistor, but in the future both wire-wound and film resistors should also also be examined.

The possibility of RF emissions from ohmic controls were observed in the driven samples. None were seen. Figure 7 shows the RF emissions in the region from 327.340 to 327.420 MHz (the D-Line region) for two ohmic (thermal) controls. There were no peaks directly associated with driving the ohmic controls even at much higher electrical input power levels. Only the original galactic background was seen unchanged from electrically driving the ohmic controls – unlike the CF/LANR components which received less than 0.1% of the power delivered to this ohmic controls and gave blazing maser outputs. What was not used for this paper was a NANOR® type component loaded with ordinary hydrogen. That must also be done in the future.

3.7. Signal generator control

Under a Faraday cage, signal generator controls were employed to check frequency and normal bandwidth. These RF intensity plots taken in the D-Line Region demonstrate the difference between the output of the signal generator (a conventional oscillator) and the NANOR®-type component. The signal generator had a Qless than 2.3×10^4. By contrast, the RF emissions obtained from the NANOR®-type component had a Q greater than 1.2×10^6 . This narrow bandwidth (high Q) heralds maser activity.

3.8. Zeeman splitting of peak by an external magnetic field

It was found that a magnetic field parallel to the major resonant cavity axis caused clear Zeeman splitting and which which decreased when the magnetic field was moved perpendicular to the major axis. This Zeeman effects/observation id consistent with reports of masers [33].

3.9. Evanescent peaks and wideband emissions

The new narrow bandwidth RF emission peaks disappear with removal of the applied voltage. Despite a much faster rise time when maser action first appears after initiating electrical drive, there is a slower fall-off of the RF emissions within several (~3–4) minutes after electrical drive is terminated. The emissions are also characterized by a much smaller amount of energy disturbed over a region of wider bandwidth. This is similar to other observed masers [34].

4. Results

4.1. RF emissions from active aqueous Ni MOAC

This experimental survey began with preliminary amateur radio and LANR investigations that examined and resolved, for the first time, the apparent absence of HL and presence of DL emissions from the MOAC LANR (ordinary water) aqueous system electrically driven during its active mode [13]. The HL and DL were regions were examined with the MOAC off over weeks, to learn the galactic (followed by the zodiac) rhythm. The initial HL results were inconclusive but with recent improvements in sensitivity and selectivity, further investigations are warranted.

The DL results showed something else. Figure 3 is composed of three curves showing the output of an aqueous $Ni/H_2OD_2O/Pt$ system MOAC-type, at three moments in time, at three moments in time; post-loading no further electrical input, electrical drive at the optimal operating point, and just beyond that input power. Figure 3 shows these RF emissions from an active aqueous Ni LANR system. The figure shows the data for experiment E31 = 180 503 with the driving power off, and then at 10 V and 45 mA electrical current, and then at 20 V and ~200 mA electrical current. Figure 3 compares the emission in the RF region between ~327.25 and ~327.5 MHz (the D-Line region) for

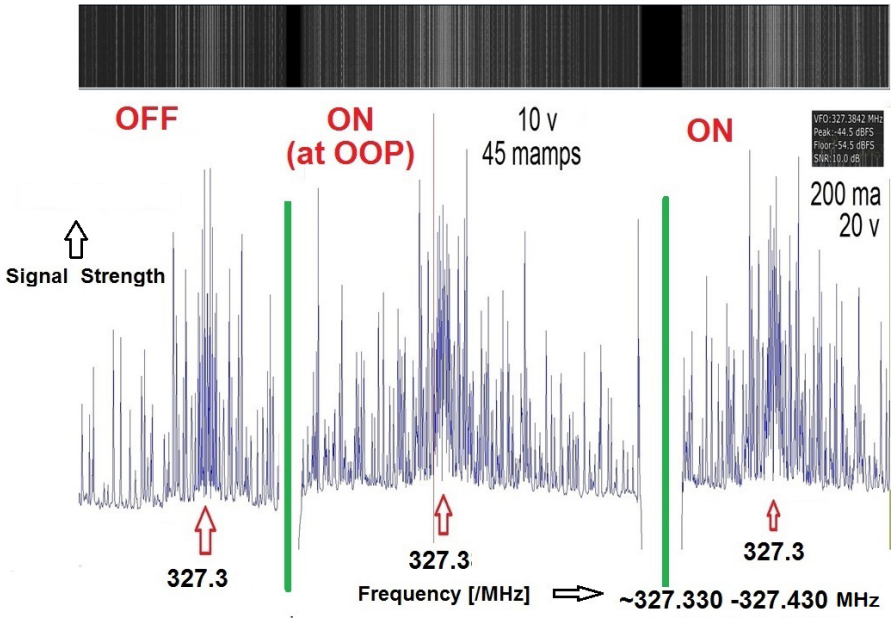

Figure 3. Comparison of the D-Line RF emissions from the aqueous MOAC in three different electrical current drives; each separated by vertical lines. The first on the left-hand side is where MOAC was OFF, after having been run for a considerable time. The second two were – at these moments – electrically driven at two input power levels. The central curve had its electrical drive point was very close to the peak of the optimal operating point (OOP) manifold [1,31].

the MOAC while off and while it was electrically driven at two levels (top of OOP [1,31]), and just to the right of the peak. The figure shows the data for Experiment E31 = 180 503 at 10 V and 45 mA electrical current.

Attention is directed to the fact that there are distinguishable differences in both the integrated amplitude near that region, and in the nature of the superhyperfine structure (sidebands). The increased emission in the D-Line region is apparent.

This is important for several reasons. First, it proves that D is the fuel. Second, the RF emission demonstrates that the deuteron, in the excited pre-^{4}He state is a D free radical. Third, the emission is normally forbidden on Earth, and here it shows up ONLY when there is excess heat. Thus, this is important because it is a signal for working, active LANR systems, providing information on the activity. For that information these sidebands are analyzed below. Because of the positive results in the aqueous system, it was also elected to further investigate the dry, preloaded NANOR®-type components for possible RF emission, too.

4.2. RF emissions from preloaded Pd NANOR®-type components

There were also positive results (analyzed below) from the dry preloaded NANOR®-type components.

Unlike the result from the ohmic resistors, there is a clear LANR-related narrow bandwidth maser line emission resulting ONLY from electrically driving some of these ZrO_2PdD preloaded Nanor® -type LANR components (7-4,7-5, and others) below the avalanche voltage (e.g. Fig. 4 and see [10,13]). These very narrow bandwidth emission peaks (some singular, and others with sidebands) are hundreds of Hertz wide in a frequency band of 327 MHz. The narrow bandwidth RF emission peaks which appear with electrical drive are located very close to the expected emission of

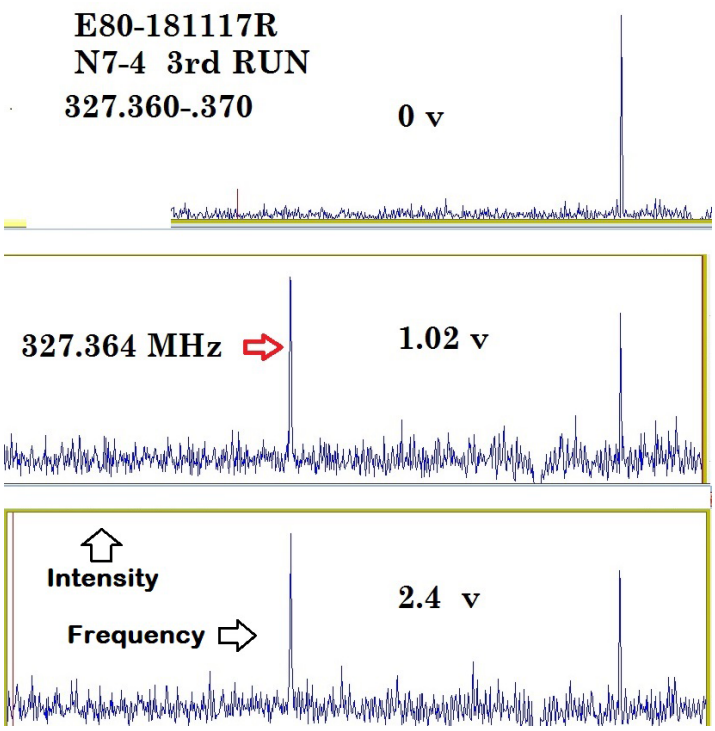

Figure 4. Appearance of maser line. Shown is the Intensity of the RF emissions in the region from 327.360 to 327.370 MHz (the D-Line region) as a function of frequency and applied electrical potential to the NANOR® type component N7-4. A high Q output is seen at 327.364 MHz. The other RF emission line on the right is galactic in origin.

deuterium.

Figures 1, 5, and 7 are the images showing the superhyperfine output a prefilled nanostructured PdD–ZrO_2 material. Figure 1 shows the instantaneous intensity vs. frequency output on top, and a waterfall image of the superhyperfine structure with intensity at various times, vs. frequency.

This is important for several reasons. First, it proves that D is also the fuel for the dry preloaded LANR components. Second, the RF DL emission again appears ONLY when there is excess heat and NOT when they are subthreshold voltage and NOT when they are in avalanche mode. As importantly, the RF maser emission and sidebands ONLY occur for several LANR components and NOT when other components are substituted for them. As with the aqueous LANR system, this is important because it is a signal for working, active nanomaterial LANR systems, providing information on the activity.

4.3. Larger voltages reveal superhyperfine line spectra

There are voltage dependent sub-hyperfine (hereinafter called “superhyperfine”) peaks. The applied voltage increase yielding this display of superhyperfine sideband structure can be seen in Fig. 5. At higher electrical input power, some peaks increase in amplitude (327.3839 MHz) and additional peaks appear. The newly appearing peaks, like the previous LANR-active RF DL peaks are evanescent when the power is turned off; and can be seen to disappear in the

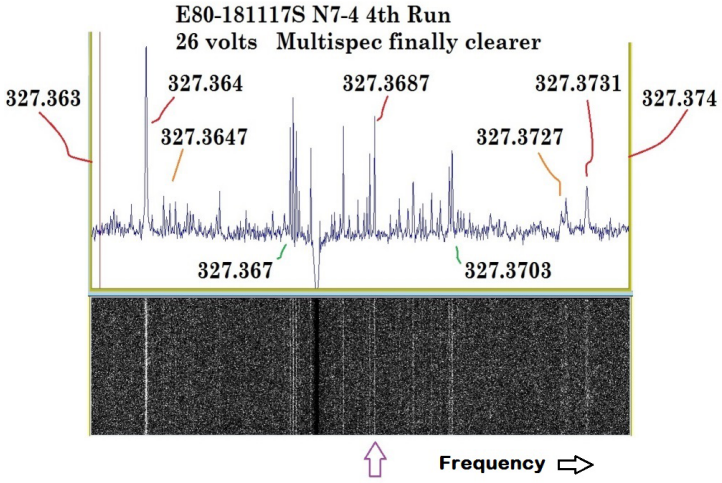

Figure 5. Superhyperfine structure of RFDL-LANR emission. This is a frequency–time plot of the driven LANR component. Note the appearance of a central maser line which is NOT the highest amplitude. Shown is the RF intensity as a function of frequency in the D-Line region for the NANOR®-type component N7-4, and increased drive potential was used to bring out the peaks. Improved grounding was used to maximally remove may other interfering signals (QRM) and atmospheric noise (QRN). The null to the right of the 327.367 MHz complex is an error in the equipment/receiver that usually is placed outside of the examined region.

lowest graph (the return to off).

It might be important to note that the RF maser emission occurred at lower driving voltages than had been used to elicit other diagnostic techniques such as CMORE spectroscopy looking for antiStokes lines. It is unclear the reason, or why higher trans-sample voltages below threshold electrical avalanche voltage, elicited the superhyperfine lines (DL sidebands) appear.

This needs to be further investigated as a function of input current, as well as power, because analysis may yield information on the collisions which lead to the desired reactions, as well as the material science.

This analysis begins with attention directed to Figures 1, 5 and 7. They show the superhyperfine structure of the RF DL-LANR emission of D-loaded Pd in its active state. It is an image showing the superhyperfine output of a prefilled nanostructured PdD–ZrO_2 material. It has an instantaneous intensity vs. frequency output of the driven active LANR component on top, and a waterfall image of the superhyperfine structure with intensity at various times, vs. frequency. Shown is the RF Intensity as a function of frequency in the D-Line region for the NANOR®-type component N7-4, and increased drive potential was used to bring out the peaks. Improved grounding was used to maximally remove may other interfering signals (QRM) and atmospheric noise (QRN). The main peak (at 327.3687 MHz) and several peaks of the superhyperfine structure (sidebands) are shown. A receiver artifact is shown. This null to the right of the 327.367 MHz complex is an error in the equipment/receiver that usually is placed outside of the examined region.

Figures 1,5, and 7 have information which enables analysis of the D-Line RF emission using the superhyperfine structure. These RF emission lines are first analyzed for symmetry (Fig. 7), and then for their amplitude and positions as a function of frequency (Fig. 1). Figure 1 is an image showing the superhyperfine output of a prefilled nanostructured PdD–ZrO_2 material, with intensity vs. frequency output on top, and two hypothetical (gendanken) exceptions of locations of said outputs when resonance broadening and location in the lattice are both considered.

Only after the LANR components are electrically driven into the active XSH-producing state, the data is collected.

The information is obtained by an analytical system which measures, or derives, the coordination numbers determined by the normalized intensities of the superhyperfine peaks, and the resonance broadening determined by the translational distance of each of the superhyperfine peaks from the central peak. This is important for at least three reasons. First, the superhyperfine structure does NOT appear when the components are at subthreshold driving voltage, and NOT when they are in electrical avalanche mode, nor when other components are substituted for them. Second, the RF emission provides unique information about the driving/controlling/limiting conditions of the desired state of active CF/LANR. Third, it yields characteristics regarding the location within the lattice.

5. Interpretation

5.1. Analysis of superhyperfine line spectra

The emissions have very narrow bandwidth. The Q (frequency over half power bandwidth) has ranged from 1.2×10^6 to some measurements at high as 9×10^6. This is because in the microwave region, at the DL line, spontaneous emission can be neglected [26] supported by the fact that atomic deuterium as occurs in Group VIII binary metals has no electric dipole moment. As in outer space, because atomic deuterium and hydrogen have no electric moment, this transition between these two states is highly forbidden with an extremely small transition rate.

It is unclear why the emission frequency is not precisely the same as for free radical deuterium. It may be perturbations of the electron orbits in D secondary to the Ni or Pd in which it is a binary alloy. It may also arise from magnetic Ni or Pd atoms which impact the hyperfine, and now superhyperfine, splitting. The Pd^{105} (abundance 22%) has a nonzero nuclear magnetic moment, and we have discussed some of these magnetic Pd effects in this magnetized LANR components [10].

This paper reports that the LANR induced RF DL-emissions yield insight into LANR active site, the LANR active excited state, and the periodic magnetic locations surrounding the RF emitter. As a result, as shown below, these energy and matter-magnetic field intensity power spectra can be analyzed to give metallurgical and material science information not otherwise available.

It is believed that the separations results because of resonance broadening which occurs when the perturbing particle is of the same type as the emitting particle and it introduces the possibility of energy exchange processes. The resonance broadening goes as $\frac{1}{r^3}$, where r is the distance from the active CF/LANR site.

Most importantly, this paper reports that the hyperfine structure of some of these LANR DL appear consistent with the RF-emitting deuteron being located in an FCC vacancy for Pd systems. This is important, and it also reveals insight into the stereoconstellation surrounding the LANR active site.

5.2. Asymmetry analysis of PdD superhyperfine structure

These RF emission lines have been analyzed first for asymmetry, and then for their amplitude and positions as a function of frequency. This analysis begins with attention directed to Fig. 7. Start with the arrow and focus on that line above the arrow: note the near mirror appearance of the singlets and the multiplet. The arrow marks appear is the actual central line around which all the lines and spacings are somewhat symmetric. Note that this is by spacing. Unlike "normal" spectroscopy, it is not symmetric by intensity. In this case, the arrow marks the central CF/LANR RF maser D-Line which is NOT the highest amplitude. The asymmetry is 7% for the 1st closest position. For the more complex range of the superhyperfine structures the variation is ~10 +/-5%. It is 13% for the third closest position.

These are actually far smaller than the 50% discussed and noted in the literature for some other Zeeman splitting [15,35].

In Fig. 6, also note that during drift towards a stable monochromatic frequency, the sidebands in the superhyperfine structure move together.

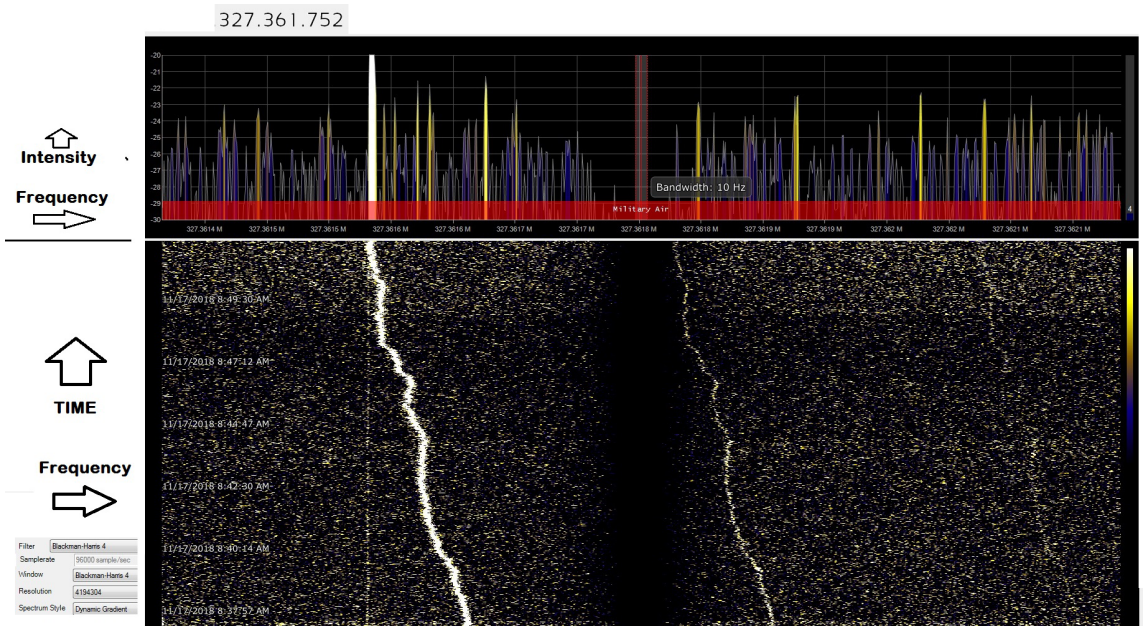

Figure 6. Connected drift of superhyperfine structure of RFDL-LANR emission. This is a frequency–time plot of a driven LANR component showing drift and shift (hunting) behavior. Shown is the RF intensity emission, before stabilization, as a function of frequency in the D-Line region for the NANOR® type component N7-4, and increased drive potential was used to bring out the peaks. Improved grounding was used to maximally remove other interfering signals and QRN.

5.3. Identification of PdD closest neighbors

Figure 1 shows that the LANR induced RF DL-emissions yield insight into LANR active site and the LANR active excited state. As a result, as shown below, these energy and matter-magnetic field intensity power spectra can be analyzed to give metallurgical and material science information not otherwise available.

Understanding the analysis of the superhyperfine structure of the D-line emission of the LANR active state begins with an examination of the closest neighbors in the palladium lattice – which is face centered cubic. Consider, within the lattice, the first four levels of closest neighbors which exist, and are now examined, around a gendanken FCC Pd vacancy. In such an FCC lattice, at any point, there are 12 first closest neighbors. They each have a distance of 1/2 lattice spacing away. Therefore, it is said that the coordination number (CN) is 12 and the separation distance, d, is a/2.

First closest neighbor CN $= 12$, $d = a/2$, where a is the lattice spacing.

Next, there are 8 s closest neighbors. These are located on opposite walls of the unit cell. The distance of separation, d, in this case, is the unit cell distance divided by the square root of two.

Second closest neighbor CN$= 8$, $d = a/\sqrt{2}$.

Then, there are six third closest neighbors. They are located one lattice space away in each of the six directions. That makes d equal to a, the lattice spacing.

Third closest neighbor CN$= 6$, $d = a$.

Finally, the fourth closest neighbors are eight in number, and located at the opposite vertices of the two units abutting the face centered cubic palladium site under analysis. In this case, the separation distance, d, is the lattice spacing

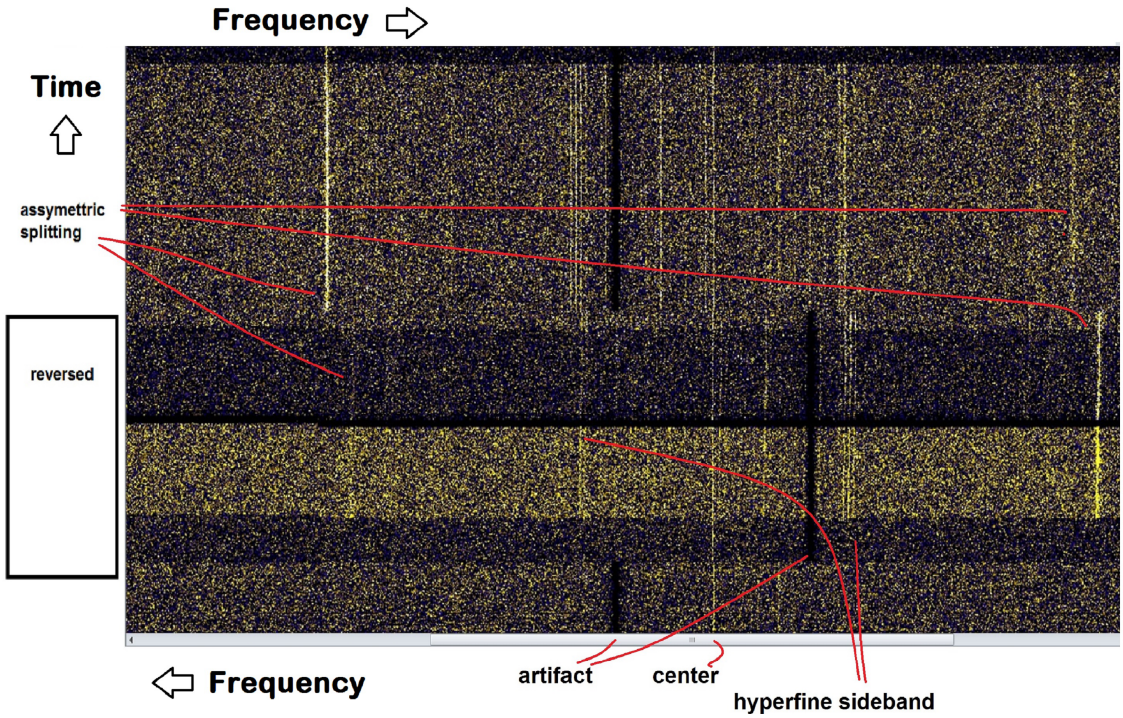

Figure 7. Asymettry analysis of Pd superhyperfine splitting. Shown is the superhyperfine spectrum of D-loaded Pd in its active state. The bottom half is optically mirror-reversed around the center, showing that there is not exact symmetry.

times the square root of 3/2.

Fourth closest neighbor CN= 8, $d = a\sqrt{3/2}$.

5.4. Impact of closest neighbors on superhyperfine spectrum

Resonance broadening occurs when the perturbing particle (in this case deuterons in other vacancies) is of the same type as the emitting particle (a deuteron emitting at the D-line), and that will introduce the possibility of an energy exchange process. Using the results of Table 1, specifically the resonance broadening (or relative magnetic field intensities depending upon the model) which should be directly proportional to the hyperfine splitting. Thus, the ratios of the impact of resonance broadening (or magnetic impact) were derived for the first four closest neighbor sites, and then superposition used.

These ratios, derived in Table 1, are shown semiquantitatively in Fig. 8 normalized to the strongest (putative closest neighbor) line. Incidentally, the variation in distance in the Column 3 should come into play in the Dicke narrowing contributing to the high Q.

Resonance broadening falls off is the cube root of the distance. Thus, the $1/r^3$ characterizes the falloff of the resonance interaction, and the constellation of these superhyperfine peaks are a means to identify, where in the lattice from where they come. This is done by examining the overlap of expected peaks/lines and actual derived peaks (superhyperfine lines) as a function of said frequency.

Thus, the ratios of RB impact were derived for the first four closest neighbor sites, and then superposition used. The first column in Table 1 are the nearest neighbors by position for Pd. The second column normalizes the lattice spacing. The third column is therefore the relative distance, followed by the coordination number in column four. The final column contains the expected resonance broadening, which like derived relative magnetic field intensities, falls off as $1/r^3$. Normalization was made to the largest observed line. Incidentally, the variation in distance in the Column 3 should come into play in the Dicke narrowing contributing to the high Q. Attention is now made to determine the lattice geometric parameters and which phase (such a FCC or BCC) the lattice is comprised.

5.5. Vacancy (FCC) is the active site

These CF/LANR-induced RF emission lines, superhyperfine lines, have been analyzed (Fig. 1). It is an image showing the superhyperfine output of a prefilled nanostructured PdD–ZrO_2 material, Nanor®-type component 7-4. The figure shows the lattice analysis of this active PdD component from its RF emission frequency-time plot.

At the top of Fig. 1 is the intensity as a function of frequency plot, in a waterfall presentation of the experimental findings by frequency horizontally, as a function of time vertically. Here, the Nanor®-type component 7-4 is driven at sufficient voltage that the additional lines appear. In the middle of Fig. 1, some of the peaks are identified. This is simplified in that, for example, the triplet is treated as a single peak. At the bottom of Fig. 1, shown are the coordination number and expected deviations by calculated resonance broadening at each putative active site based upon known locations for both FCC and BCC lattice arrangements. The expected resonance broadening has falloff which does decrease as $1/r^3$.

Attention is directed to the two hypothetical (gendanken) expectations of locations of said outputs when resonance broadening and location in the lattice are both considered for a FCC lattice vs. a BCC lattice, for comparison. Each compares the expected findings for four nearest neighbors. Each has the horizontal distance related to the inverse cube of the distance, d. Also shown is the coordination number, for each. The figure shows considerable overlap of the expected locations in the mid-graph and the frequency singularities above them for the FCC lattice, but not the BCC lattice. The FCC locations and BCC locations respectively must be compared with what is observed. The normalizations for each are made for the first closest neighbor.

FCC is a much closer match than BCC, and thus the actual lattice of Pd heralds the location of the active site. Thus, most importantly, analysis of the amplitude and positions as a function of frequency of the superhyperfine structure of these LANR DL emissions appear consistent with the RF-emitting deuteron being in an excited atomic state and being in a slightly modified palladium (Pd) vacancy within the Pd FCC lattice vacancy. This is important, and it also reveals insight into the stereoconstellation surrounding the LANR active site. The data uniquely shows the positions of nearby sites vicinal to an emitter, and they appear to be at nearest neighbor FCC locations, which closely match what is observed (Fig. 1). Simply put, the results in Fig. 8 show that the palladium vacancy is, as predicted at ICCF-4 (Swartz), the site of the desired reaction in these active systems.

Furthermore, for the lower RF frequencies, there is another indication that the coordination number is qualitatively

Table 1. Impact of resonance broadening from nearest neighbor locations in Pd FCC normalized to the first closest neighbor.

Nearest neighbor	Spacing	Rel distance to vacancy	CE coordination number	Rel. resonance broadening field intensity at DL emission location
First	1	0.50	12	1
Second	1	0.7072	8	0.3533
Third	1	1.0	6	0.125
Fourth	1	1.2248	8	0.06801

associated with what is seen. The output qualitatively appears to match the intensity of some of the lines for the FCC lattice.

If the magnitudes of the received outputs are qualitatively related to the expected emissions by coordination number, then the band at 327.364 MHz (blue band) is in fact the largest at the lower frequencies, as expected. This may explain why the center peak is NOT the highest in magnitude (unlike Zeeman splitting).

5.6. Other changes observed in ZrO_2–PdD

5.6.1. *Fourth closest neighbor merged with second closest neighbor*

Furthermore, upon close inspection, the spectra provide information on the interactions between active sites, in situ. Specifically, the lower RF frequencies also suggest that the coordination number is qualitatively associated with what is seen – except for the following.

The second closest neighbors are now different. Also this comes from interaction with half of the fourth closest neighbors. Analysis of the superhyperfine structure is consistent with what appears to be loss of coordination number (CN) meaning a change in structure with fewer in that position and some of the elsewhere including a new interaction causing an apparent change in magnetic properties of, the fourth and second closest neighbors, respectively (Figs. 1 and 7). Specifically, it appears that part of the fourth nearest neighbors are now interacting with the second closest neighbors creating a superhyperfine structure within (green band).

5.6.2. *Third closest neighbor demonstrates multiplet substructure*

The superhyperfine structure indicates a multiplet at the position of, and possibly due to a new, second nearest neighbor. This might mean that this results from the active site being near, or in, the zirconium oxide, at a rhombic corner. That location is magnetically closely isoequivalent to an FCC vacancy (Fig. 1). Alternatively, it might mean that an atom of zirconium (or impurity therein the oxide) may have entered the Pd lattice, as has been suggested [30].

5.7. Analysis of non-Zeeman superhyperfine splitting for NiD

The RF emission lines have been analyzed more closely of the data derived from the aqueous nickel MOAC system in its active mode (Figs. 9 and 10). Figure 9 shows the asymmetry analysis. It is much closer to a theoretical mirror, than for the Pd system.

5.8. Identification of NiD closest neighbors

Figure 10 shows the experimental findings on the top. This presents the data by frequency horizontally, as a function of time vertically. The graph on the bottom shows the expected relative resonance effect (or alternatively magnetic field intensity) for each of the closest neighbors, and has the horizontal distance related to the inverse cube of the distance, d , for BOTH an FCC lattice, and BCC lattice. Analysis of the amplitude and positions as a function of frequency strongly suggest that the hydride nickel has changed in phase from a simple FCC lattice.

The data uniquely shows the nearby sites surrounding the active site in an active nickel CF/LANR system. Note that some locations appear to have further splitting, and there are what appear to be two slightly different layers within the new phase, or two new phases.

The minority report must include that the vacancy might be in rhombic ZrO_2 which is also an FCC.

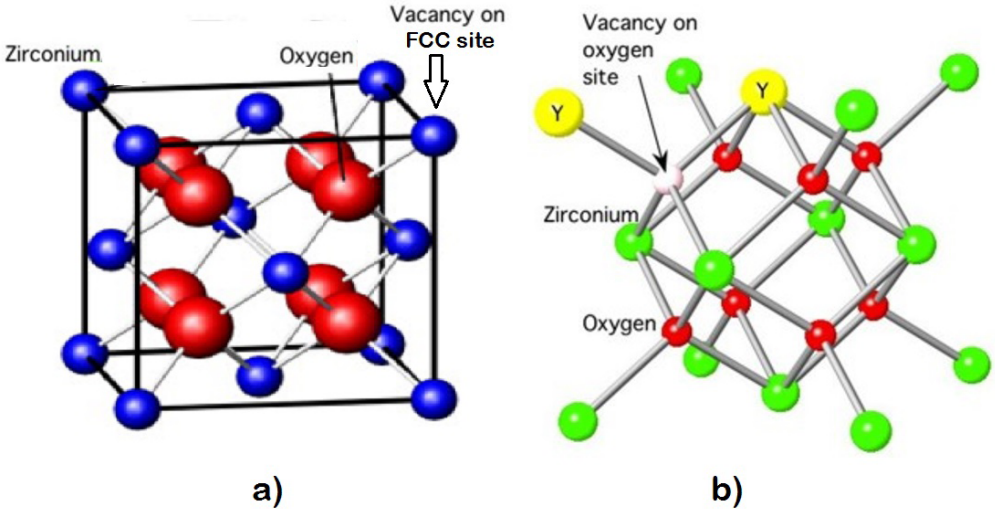

Figure 8. Possible vacancy sites to consider on ZrO_2. The first possible site is in the rhombic formation, which is near FCC in stereoconstellation (*left*). Oxygen vacancies should be considered even though inconsistent with the present group of sidebands (superhyperfine lines; *right*).

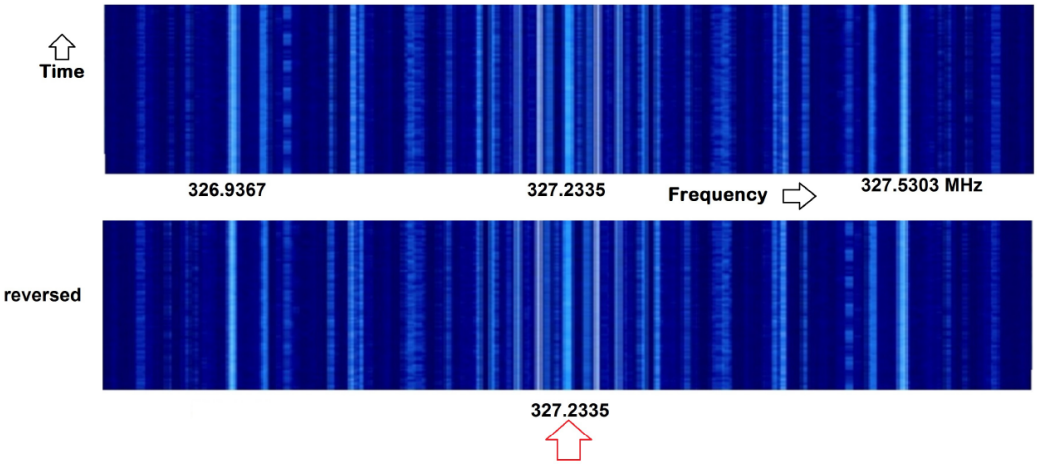

Figure 9. Asymmetry analysis of nickel superhyperfine splitting. Shown is the superhyperfine DL spectrum of the hydrogen loaded nickel MOAC in its active state (40 V, 200 mA). Note that the bottom half is simply reversed horizontally around the arrow to enable comparison of the left and right. The frequencies of the widest, and central, peaks are identified. For both cases, in this instance, the center is identified by the arrow. Attention is directed to the symmetry.

6. Conclusions

Active CF/LANR systems, both aqueous and nanomaterial, emit very narrow bandwidth RF emission peaks (ca. 327.37 MHz), which are located very close to the theoretical Deuteron-Line (DL; 327.348 MHz) region, and they exhibit a large Q ($>1.2 \times 10^6$), which is the ratio of the bandwidth at half power to the frequency [13]. This paper demonstrates that at higher applied driving voltage, a superhyperfine line structure of sidebands appears, and this revelation gives more insight into the volume and stereoconstellation around the active site.

6.1. Confirmation of fuel

These results confirm that in active CF/LANR systems deuterons are making helium-4 which generates the observed excess energy in the active state [17,37]. This excess energy has a very large specific density making it comparable to other systems [38]. The fuel generates the fusion product and at least some of these reactions occur in face center cubic (Pd FCC) vacancy for palladium (in PdD) or Zr (in ZrO_2).

6.2. Derivation of the active site

Analysis using putative nearest neighbors indicates a possible location of the deuteron free radical during its RF emission. Vacancies, as predicted at ICCF-4 [16], are apparently the site of some of the desired reaction in these active systems. The coordination number is qualitatively associated with what is seen, except for some possibly very important changes. The second closest neighbors are now different. And this appears to have come from interaction with half of the fourth closest neighbors, with either that interaction of additional paramagnetic (possible lattice Zr in Pd contamination) factors, changing the singlet to multiplet.

The results in nickel are much more complex and demonstrate a range of both FCC and BCC vacancies, possibly heralding new metallurgic phases.

6.3. Summary

Detection, RF identification and recognition of LANR RF emission from the active state are important. The reasons include information about the activity, location of, and changes to, the active site.

In the future, RF detection, like coherent antiStokes spectroscopy [11,12,32], can be used to detect the active – rate-limiting–excited (desired) state. These also discern data from the phenomenon's location, including some of the conditions requisite to attain the desired active XSH-producing driven state.

In the next paper [14], another important detail of the superhyperfine line structure of sidebands will be discussed. It appears that in active CF/LANR systems, the loaded deuterons work together from their vacancy sites, disappearing two at a time from those deuterons decorating the binary alloy, to enable continuation of the desired XSH-producing reactions within the loaded Group VIII metal. At least some of their emitting RF radiation superhyperfine line peaks, located at the DL heralding the inverted population, are observed to be pulsing. This action may herald quantum movements of energy and matter within an active XSH-producing PdD Lattice.

Acknowledgments

The author gratefully acknowledges and thanks David Nagel, Bo Gardmark, Gayle Verner, Peter Hagelstein, Lawrence Forsley, Louis Dechiaro, Isidor Straus, Joshua Gyllinsky, Brian Ahern, John Wallace and Dan Steinberg for their very helpful comments, editorial assistance, and additional material. The author also thanks Brian Ahern, Alan Weinberg and the late Charles W. Haldeman for their construction, early testing, modifications, and transfer of the MOAC. This effort has been supported by JET Energy Inc., Nanortech Inc., and Anthropocene Institute.

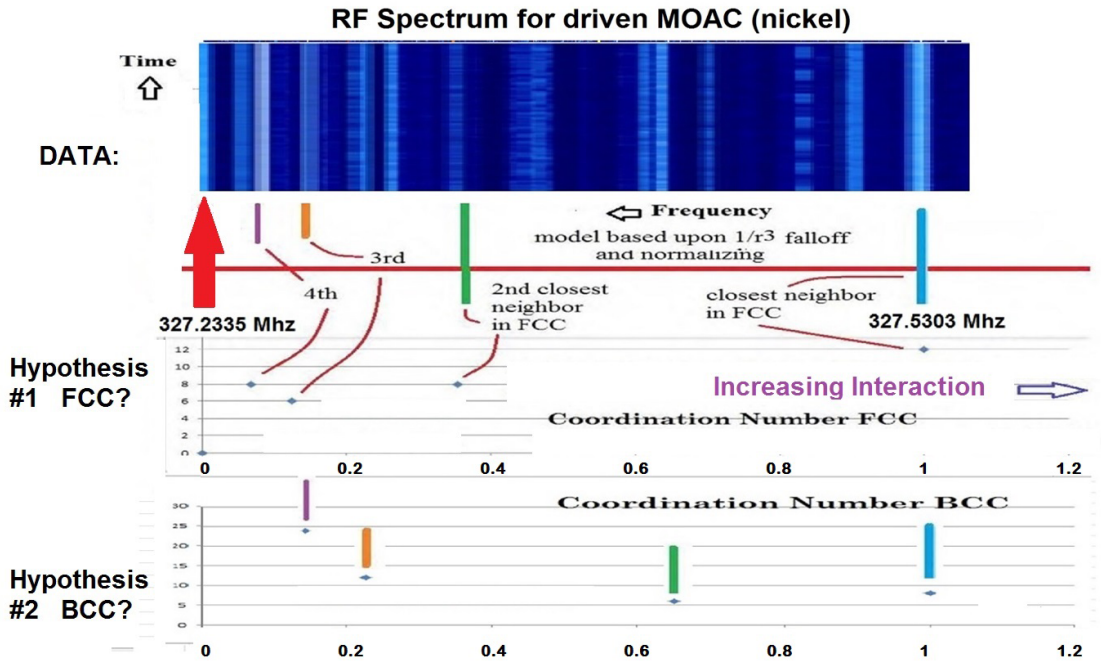

Figure 10. Lattice analysis of active MOAC's frequency–time plot. This figure shows an analysis of the active MOAC's (nickel cathode) super-hyperfine structure using a frequency–time plot and, below it, implied assignment based upon nearest neighbor location and the expected magnetic field intensity (falloff–$1/r^3$ model). *Top*: Intensity as a function of frequency in a Waterfall. Here, the MOAC is electrically driven to produce excess power. Middle: Some of the peaks (those for FCC, for simplicity) identified. *Bottom*: Coordination number and expected deviation for each calculated magnetic field strength at the putative active site based upon known locations for both FCC and BCC lattice arrangements. The figure shows considerable overlap of the expected locations for the FCC lattice, and the BCC lattice. This may be consistent with the new phases seen for electrochemically loaded nickel [36].

References

[1] M.R. Swartz, G. Verner and J. Tolleson, Energy gain from preloaded ZrO_2–PdNi–D nanostructured CF/LANR quantum electronic components, *J. Condensed Matter Nucl. Sci.* **13** (2014) 528, www.iscmns.org/CMNS/JCMNS-Vol13.pdf.

[2] M.R. Swartz, G. Verner, J. Tolleson and P. Hagelstein, Dry, preloaded NANOR®-type CF/LANR components, *Current Sci.* **108** (4) (2015) 595.

[3] M.R. Swartz and P.L. Hagelstein, Demonstration of energy gain from a preloaded ZrO_2–PdD nanostructured CF/LANR quantum electronic device at MIT, *J. Condensed Matter Nucl. Sci.* **13** (2014) 516, www.iscmns.org/CMNS/JCMNS-Vol13.pdf.

[4] M.R. Swartz, P.L. Hagelstein and G. Verner, Impact of electrical avalanche through a ZrO_2–NiD nanostructured CF/LANR component on its incremental excess power gain, ICCF-19, *J. Condensed Matter Nucl. Sci.* **19** (2016) 287–297.

[5] M.R. Swartz, Optical detection of phonon gain distinguishes an active cold fusion/LANR component, *J. Condensed Matter Nucl. Sci.* **20** (2016) 29–53, www.iscmns.org/CMNS/JCMNS-Vol20.pdf.

[6] M.R. Swartz and P.L. Hagelstein, Increased PdD anti-Stokes peaks are correlated with excess heat mode, *J. Condensed Matter Nucl. Sci.* **24** (2017) 130–145.

[7] M.R. Swartz, G. Verner, J. Tolleson, L. Wright, R. Goldbaum and P.L. Hagelstein, Imaging of an active NANOR®-type LANR component using CR-39, *J. Condensed Matter Nucl. Sci.* **15** (2015) 81, www.iscmns.org/CMNS/JCMNS-Vol15.pdf.

[8] M.R. Swartz, Incremental high energy emission from a ZrO_2–PdD nanostructured quantum electronic component CF/LANR,

J. Condensed Matter Nucl. Sci. **15** (2015) 92, www.iscmns.org/CMNS/JCMNS-Vol15.pdf.
[9] M.R. Swartz, G. Verner, J. Tolleson, L. Wright, R. Goldbaum and P.L. Hagelstein, Amplification and restoration of energy gain using fractionated magnetic fields on ZrO_2–PdD nanostructured components, *J. Condensed Matter Nucl. Sci.* **15** (2015) 66, www.iscmns.org/CMNS/JCMNS-Vol15.pdf.
[10] M.R. Swartz, P.L. Hagelstein and G. Verner, Impact of electrical avalanche through a ZrO_2–NiD nanostructured CF/LANR component on its incremental excess power gain, ICCF-19, *J. Condensed Matter Nucl. Sci.* **19** (2016) 35–46.
[11] M.R. Swartz, Optical detection of phonon gain distinguishes an active cold fusion/LANR component, *J. Condensed Matter Nucl. Sci.* **20** (2016) 29–53, www.iscmns.org/CMNS/JCMNS-Vol20.pdf.
[12] M.R. Swartz and P.L. Hagelstein, Increased PdD anti-Stokes peaks are correlated with excess heat mode, *J. Condensed Matter Nucl. Sci.* **24** (2017) 130–145.
[13] M.R. Swartz, Deuterons in active LANR systems emit a 327.37 MHz hyperfine maser line, *J. Condensed Matter Nucl. Sci.* (2019), to appear.
[14] M.R. Swartz, Pulsatile 327.37 MHz superhyperfine line heralds lattice mass–energy movements, *J. Condensed Matter Nucl. Sci.* (2019), to appear.
[15] G.W. Walker, On asymmetry of the Zeeman effect, The London, Edinburgh, and Dublin Philosophical Magazine, *J. Sci. Series 6* **3** (14) (1902) 247–251, https://doi.org/10.1080/14786440209462760.
[16] M.R. Swartz, Catastrophic active medium (CAM) theory of cold fusion, *Proc. ICCF4,* 4, 1993, p. 255, sponsored by EPRI and the Office of Naval Research.
[17] M.R. Swartz, Charles Haldemann, Alan Weinberg and Brian Ahern, Possible deuterium loss during excess heat from ordinary water-carbonate electrolyte using nickel, *J. Condensed Matter Nucl. Sci.* **29** (2018) 169.
[18] M.R. Swartz, Aqueous and nanostructured CF/LANR systems each have two electrically driven modes, *J. Condensed Matter Nucl. Sci.* **29** (2019) 177.
[19] M.R. Swartz, Consistency of the biphasic nature of excess enthalpy in solid state anomalous phenomena with the quasi-1-dimensional model of isotope loading into a material, *Fusion Technol.* **31** (1997) 63–74.
[20] M.R. Swartz, Codeposition of palladium and deuterium, *Fusion Technol.* **32** (1997) 126–130.
[21] M.R. Swartz and G. Verner, Excess heat from low electrical conductivity heavy water spiral-wound Pd/D_2O/Pt and Pd/D_2O–$PdCl_2$/Pt devices, *Condensed Matter Nuclear Science, Proc.ICCF-10*, World Scientific, NJ, ISBN 981-256-564-6, 29-44; 45-54 (2006).
[22] M.R. Swartz and G. Verner, The Phusor®-type LANR cathode is a metamaterial creating deuteron flux for excess power gain, *Proc. ICCF-14,* Vol. 2, D.J. Nagel and M.E.Melich (Eds.), 2008, p. 458, ISBN: 978-0-578-06694-3, 458, (2010); www.iscmns.org/iccf14/ProcICCF14b.pdf.
[23] M.R. Swartz, G. Verner and A. Weinberg, Non-thermal near-IR emission from high impedance and codeposition LANR devices, *Proc. ICCF14,* Vol. 1, D.J. Nagel and M.E.Melich (Eds.), 2008, p. 343, ISBN: 978-0-578-06694-3, 343, (2010); www.iscmns.org/iccf14/ProcICCF14a.pdf.
[24] M.R. Swartz, Excess power gain using high impedance and codepositional LANR devices monitored by calorimetry, heat flow, and paired stirling engines, *Proc. ICCF14* **1** (2008) 123, ISBN: 978-0-578-06694-3, 123, (2010), www.iscmns.org/iccf14/ProcICCF14a.pdf.
[25] M.R. Swartz, Survey of the observed excess energy and emissions in lattice assisted nuclear reactions, *J. Scientific Explor.* **23** (4) (2009) 419–436.
[26] M. Swartz, Improved electrolytic reactor performanceusing π-notch system operation and gold anodes, Transactions of the American Nuclear Association, Nashville, TN, Meeting, ISSN:0003-018X publisher LaGrange, Ill, Vol. 78, 1998, 84–85.
[27] M. Swartz, Can a Pd/D_2O/Pt device be made portable to demonstrate the optimal operating point?, Condensed Matter Nuclear Science, *Proc. ICCF-10*, P.L. Hagelstein and S.R. Chubb (Eds.), World Scientific, NJ, ISBN 981-256-564-6, 29-44; 45-54 (2006).
[28] M. Swartz, Investigations of heat after death: analysis of factors which determine the tardive thermal power and HAD enthalpy, *J. Condensed Matter Nucl. Sci.* **31** (2020) 20–41.
[29] M. Swartz, Photoinduced excess heat from laser-irradiated electrically-polarized palladium cathodes in D_2O, Condensed Matter Nuclear Science, *Proc. ICCF-10*, P.L. Hagelstein and S.R. Chubb (Eds.), World Scientific, NJ, ISBN 981-256-564-6, 213-226 (2006).

[30] M. Swartz, G.M. Verner and A.H. Frank, *The Impact of Heavy Water (D_2O) on Nickel-Light Water Cold Fusion Systems*, *Proc. ICCF9*, Xing Z. Li (Ed.), China, 2002, pp. 335–342.

[31] M.R. Swartz, Optimal operating point manifolds in active, loaded palladium linked to three ditinct physical regions, *Proc. ICCF-14*, Vol. 2, D.J. Nagel and M.E.Melich (Eds.), 2008, pp. 639, ISBN: 978-0-578-06694-3, 639, (2010).

[32] M.R. Swartz, Increase of an anti-stokes peak at the cathode of an electrically-driven, active aqueous nickel/H_2O/Pt system, *J. Condensed Matter Nucl. Sci.* **279** (2018) 22.

[33] R.L. Plante, K.Y. Lo, R.M. Crutcher and N.E.B. Killeen, The magnetic field at the galactic center: detection of HI Zeeman splitting, American Astronomical Society, 183rd AAS Meeting, id.116.05, *Bull. Amer. Astronomical Soc.* **25** (1993) 146, 7AAS...18311605P.

[34] D.J. Wineland and N.F. Ramsey, Atomic deuterium maser, *Phys. Rev*. A **5** (1972) 821.

[35] J.E. Mack and O. Laporte, Asymmetric Zeeman effect patterns in a complex spectrum, *J. Archive, Phys. Rev.* **51** (1937) 291, DOI:https://doi.org/10.1103/PhysRev.51.291.2.

[36] M.R. Staker, Coupled calorimetry and resistivity measurements, in conjunction with an emended and more complete phase diagram of the palladium – isotopic hydrogen system, *ICCF-21*,
June 5, 2018, https://www.youtube.com/watch?v=4FeMnRjTtr0.

[37] M. Miles, Correlation of excess power and helium production during D_2O and H_2O electrolysis using palladium cathodes, *J. Electroanal. Chem.* **346** (1993) 99–117.

[38] M.R. Swartz, Comparison of NANOR-type LANR components to ^{238}Pu as a heat source for space flight, *J. Condensed Matter Nucl. Sci*. **29** (2019) 238.